Li zoning in zircon as a potential geospeedometer and peak temperature indicator

Contrib Mineral Petrol (2016) 171:25
DOI 10.1007/s00410-016-1238-8

ORIGINAL PAPER

Li zoning in zircon as a potential geospeedometer and peak temperature indicator

Dustin Trail[1] · Daniele J. Cherniak[2] · E. Bruce Watson[2] · T. Mark Harrison[3] · Benjamin P. Weiss[4] · Ian Szumila[1]

Received: 8 October 2015 / Accepted: 30 January 2016 / Published online: 25 February 2016

Abstract Zircon Li concentrations and δ^7Li values may potentially trace crustal recycling because continental and mantle-derived zircons yield distinct values. The usefulness of these differences may depend upon the retentivity of zircon to Li concentrations and isotopic ratios. Given the relatively high Li diffusivities measured by Cherniak and Watson (Contrib Mineral Petrol 160: 383–390, 2010), we sought to discover the scenarios under which Li mobility might be inhibited by charge-compensating cations. Toward this end, we conducted "in" diffusion experiments in which Li depth profiles of synthetic Lu-doped, P-doped, and undoped zircon were determined by nuclear reaction analysis. In separate experiments, Li was ion-implanted at depth within polished natural zircon slabs to form a Gaussian Li concentration profile. Diffusively relaxed concentration profiles were measured after heating the slabs to determine diffusivities. In all experiments, which ranged from 920 to 650 °C, calculated diffusivities are in agreement with a previously established Arrhenius relationship calibrated on trace-element-poor Mud Tank zircon. Our revised Arrhenius relationship that includes both datasets is:

$$D_{\mathrm{Li}} = 9.60 \times 10^{-7} \exp\left[\frac{-278 \pm 8 \text{ kJ mol}^{-1}}{\mathrm{RT}}\right] \mathrm{m}^2\ \mathrm{s}^{-1}$$

We also observed that synthetic sector-zoned zircon exhibits near-step-function Li concentration profiles across sectors that correlate with changes in the rare earth element (REE) and P concentrations. This allowed us to examine how Li diffusion might couple with REE diffusion in a manner different than that described above. In particular, re-heating these grains revealed significant Li migration, but no detectable migration of the rare earth elements. Thus, unlike most elements in zircon which are not mobile at the micrometer scale under most time–temperature paths in the crust, Li zoning, relaxation of zoning, or lack of zoning altogether could be used to reveal time–temperature information. Discrete ~10 μm concentration zones of Li within zircon may be partially preserved at 700 °C for tens to hundreds of years, and at 450 °C for millions of years. In this regard, Li zoning in zircon holds significant potential as a geospeedometer, and in some instances as a qualitative indicator of the maximum temperature experienced by the zircon.

Keywords Zircon · Geospeedometer · Hadean · Li · Diffusion

Communicated by Othmar Müntener.

Electronic supplementary material The online version of this article (doi:10.1007/s00410-016-1238-8) contains supplementary material, which is available to authorized users.

✉ Dustin Trail
dtrail@ur.rochester.edu

[1] Department of Earth and Environmental Sciences, University of Rochester, Rochester, NY 14627, USA

[2] Department of Earth and Environmental Sciences, Rensselaer Polytechnic Institute, Troy, NY 12180, USA

[3] Department of Earth, Planetary and Space Sciences, University of California, Los Angeles, Los Angeles, CA 90095, USA

[4] Department of Earth, Atmospheric, and Planetary Sciences, Massachusetts Institute of Technology, 77 Massachusetts Avenue, Cambridge, MA 02139, USA

Introduction

The last 15 years have seen significant advances in our understanding of the trace element and isotopic character of zircon, as zircon analysts have proposed links between the

chemical characteristics of the mineral and physical processes (Wilde et al. 2001; Mojzsis et al. 2001; Watson and Harrison 2005; Harrison et al. 2008; Ushikubo et al. 2008; Trail et al. 2011a; Grimes et al. 2015). This success has been bolstered, in part, by a wide array of laboratory-based zircon trace element diffusion studies such as the rare earth elements (REEs), Ti, U, Th, and Pb, which have shown that the mobility of these elements by diffusion-related processes is exceptionally slow (Cherniak et al. 1997a, b; Cherniak and Watson 2001, 2007). For instance, the characteristic diffusive length scale ($[4D{\cdot}t]^{1/2}$ D = diffusivity, t = time) of Pb and Ti in response to 650 and 865 °C thermal events (respectively) lasting 1 Myr is just ~1 nm. Given the physical and chemical robustness of this mineral, new zircon-based tracers that track crustal evolution are under active development. The Li concentration and δ^7Li in zircon, for example, have emerged as potentially important tracers of crustal recycling, and possibly the chemical and thermal features of zircon source melts (Ushikubo et al. 2008; Bouvier et al. 2012; Li et al. 2011; Grimes et al. 2011; Rubin et al. 2014).

In the first study of its kind Ushikubo et al. (2008) reported Li concentrations and isotope ratios in zircons. Lithium contents in zircons presented in this study yielded a concentration range of ~6 orders of magnitude (~low ppb-levels to 250 ppm), and importantly, continental crust-derived zircon exhibits distinctly higher Li concentrations (10–250 ppm) when compared to mantle-derived zircons (~2 ppb or less). Thus, the high Li contents reported for Jack Hills zircons were interpreted to mean that the Hadean zircons were not derived from primitive mantle-derived magma sources. In addition, it is well known that weathered products of the crust exhibit negative δ^7Li values when compared to those obtained from mantle-derived magmas. Fresh peridotites and normal mid-ocean ridge basalts (N-MORB) typically fall in a relatively restricted range (δ^7Li 3.8 ± 1.5 ‰), relative to the international Li standard, NIST SRM-8545 (Chan et al. 1992; Elliott et al. 2006; Jeffcoate et al. 2007; Magna et al. 2006; Seitz et al. 2004; Tomascak et al. 2008). Highly fractionated δ^7Li values (−20 to +15 ‰) were measured in Jack Hills zircons by Ushikubo et al. (2008); negative values are consistent with extensive weathering during the Hadean and Archean. Ushikubo et al. (2008) also conducted ion imaging of Li in zircon and found a variably patterned correlation between Li concentrations and growth zoning, where the latter was revealed by cathodoluminescence (CL) images. Since CL growth zoning in zircon is generally attributed to the presence of certain REEs, the authors inferred that Li enters into the zircon lattice by the substitution $REE^{3+} + Li^{+} \rightarrow Zr^{4+}$. Rare earths diffuse slowly in crystalline zircon (Cherniak et al. 1997a), and for this reason Ushikubo et al. (2008) concluded that Li mobility in zircon was inhibited because of the need for charge compensation. That is, Li is fixed in the zircon structure by coupled substitutions and is rate-limited by diffusion of the REEs. Bouvier et al. (2012) reported δ^7Li, Li contents, and trace elements in zircons from a TTG (tonalite, trondhjemite, and granodiorite) and sanukitoid plutons from the Superior Province in Canada. These authors sought to establish the Li concentration and isotopic character of zircons from Archean granitoids; they discovered that Li contents of these zircons were significantly higher than those of zircons from primitive rock types such as the oceanic crust, consistent with other work (Grimes et al. 2011). These samples did not yield an abundant component of negative δ^7Li values, as did the Jack Hills samples, which suggests limited or no incorporation of negatively sourced δ^7Li-weathered material into the source melts. In addition, these authors suggested that magmatic zircons had an atomic ratio (Y + REE)/(Li + P) = 1.0 ± 0.7 (2 SD variation), supporting the hypothesis that Li is structurally accommodated in the zircon lattice by charge compensation with a REE (or Y).

Given the importance of such studies for inferring the origins and petrogenesis of rocks in the Archean and Hadean, Cherniak and Watson (2010) presented diffusion data for Li in zircon to evaluate retention of this element. These workers reported three types of experiments from 703 to 1151 °C. First, Li diffusion experiments in zircon were conducted at 1 atm under anhydrous conditions with spodumene [$LiAl(SiO_3)_2$] as the Li source material. The second style of experiments was similar, except that Dy_2O_3 was added to the source material in order to investigate the effect of possible REE + Li charge-compensating mechanisms when REEs are present in the source material of the diffusion experiment. And finally, piston cylinder experiments (at 1.0–1.2 GPa) explored Li diffusion in a fluid consisting of CO_2 and H_2O. In all cases, polished slabs of trace-element-poor Mud Tank zircon were used for the diffusion experiments. For these three types of experiments, no differences were observed in the diffusivities, and these workers were able to model the retention of Li in zircon under different hypothetical time–temperature–grain size scenarios. These calculations revealed that zircons will be moderately retentive of Li if grains are subjected to mid-crustal metamorphism; for instance, a zircon with a 50-μm radius will retain Li signatures at the grain center for a heating event of 500 °C for up to 15 Ma. In this calculation, it is assumed that Li diffusion does not depend on a charge-compensating cation, such as a REE. While the data presented by Cherniak and Watson (2010) show that Li diffusion is significantly faster than REEs, these workers did not specifically evaluate the effect of REE concentration and substitution for Li diffusion in zircon beyond the use of a REE-doped source material in one of their experiments.

Given the complexities that can arise during diffusion of Li in minerals (Dohmen et al. 2010; Richter et al. 2014), the present study seeks to fill this gap in knowledge. We present

a series of diffusion experiments from chemically diverse synthetic zircon starting materials, in order to evaluate potential rate-limiting scenarios and to evaluate whether Li concentration gradients in zircon might serve as a reliable geospeedometer and peak temperature indicator for chemically diverse zircons. Specifically, does Li migrate independently of REEs, or are Li atoms inhibited from diffusing because of REEs? And finally, we were motivated to undertake this study because it is possible that the Jack Hills zircons and their ferromagnetic mineral inclusions may enable researchers to investigate the time of origin and earliest intensity of the Hadean magnetic field, as long as the ferromagnetic carriers within zircon have not been heated above their Curie point. If magnetite is the magnetic carrier in zircon, then we would need to establish that a Hadean zircon did not reach temperatures in excess of 580 °C after primary igneous crystallization. In principle, knowledge of Li diffusion as a function of temperature could make this possible, provided Li mobility is largely independent of the concentrations of other impurities.

Methods and experimental overview

Depth profile in-diffusion studies for chemically diverse zircons

Most of our diffusion work was conducted by depth profiling with nuclear reaction analysis (NRA) using the reaction $^{7}Li(p,\gamma)^{8}Be$. This technique can provide quantitative Li concentration versus depth information at the nanometer scale, provided a flat area of the crystal surface exceeding ~1 × 1 mm is available. In order to meet the surface area requirement as well as the main goal of the project—that is, to measure Li diffusivities in zircons containing various impurities—we grew zircons by a technique known as the flux method (e.g., Chase and Osmer 1966; Suzuki et al. 1992; Hanchar et al. 2001). Our starting base mix composition consisted of a mixture of MoO_3–Li_2CO_3–$ZrSiO_4$ in a ratio of ~1 to 0.18 to 0.06 by weight; the goal was to produce three different types of zircons into which we could then diffuse Li and depth profile by the NRA technique. The first involved zircon synthesis that was conducted without the addition of trace element impurities, which resulted in nearly stoichiometric zircon. The second and third batches were separately doped with ~300 ppm P and 1300 ppm Lu, respectively. Starting mixes were firmly packed into Pt crucibles, suspended, and soaked in a 1 atm furnace at ~1400 °C for 3 h. Subsequently, samples were cooled at a rate of 3°/h to ~900 °C. Following synthesis, zircons were readily freed of residual flux material by ultrasonic cleaning. Recovered zircons were oriented along a crystallographic axis, polished with 1 μm alumina, and then finished with colloidal silica.

Finished crystals were placed in silica tubes, tightly packed with Li source material spodumene, and then vacuum-sealed before placing the samples in a 1 atm furnace at the desired temperature (~850–920 °C) and duration. Temperature was monitored with a type K thermocouple, with temperature uncertainties of approximately 2 °C. After the diffusion experiment, crystals were carefully removed and then thoroughly cleaned in successive ethanol and water baths before NRA analysis. NRA analysis was conducted following the technique described in Cherniak and Watson (2010) with a Li detection limit of ~20 ppm at. Briefly, this involved the reaction $^{7}Li(p, \gamma)^{8}Be$ and a 441-keV resonance (D'Agostino et al. 1978; Raisanen and Lappalainen 1986), and the depth profiles were obtained by varying beam energy to measure Li at greater depths in the sample. Energy steps of 2–3 keV were used initially, and energy steps were increased to 5–10 keV at depth within the zircon crystal. The gamma rays produced in the reaction were detected with a bismuth germanate detector. Specimens of spodumene were also analyzed as standards for determining Li concentrations in zircon, and, along with Al foil standards, for use in calibration of gamma energy spectra. In addition, samples of untreated zircon were analyzed to evaluate background levels in the gamma energy region of interest. The depth scales were calculated from the difference between the incident beam energy and the resonance energy, which was divided by the energy loss per unit depth in zircon for protons of this energy range, as determined from the SRIM-2006 software package of Ziegler and Biersack (2006).

For the in-diffusion experiments, diffusion was modeled as a one-dimensional, concentration-independent diffusion in a semi-infinite medium with a source reservoir maintained at constant concentration at the zircon surface. The solution for these boundary conditions is:

$$C(x,t) = C_{o}\mathrm{erfc}\left(\frac{x}{\sqrt{4Dt}}\right) \quad (1)$$

where C is the concentration of Li in zircon at time t and distance x from the polished surface, C_o is the surface concentration, and D is the diffusivity (Crank, 1975).

We evaluated diffusivities by plotting the inverse of the error function; that is, $\mathrm{erf}^{-1}((C_o - C(x,t))/C_o)$ versus depth (x). In the case of in-diffusion into a semi-infinite reservoir as described here, the result should be a straight line with a slope of $(4D{\cdot}t)^{-1/2}$. The uncertainties in concentration and depth were used to propagate uncertainties to the calculated diffusivities. All diffusivities and errors were fit using Origin 9.1® software package.

After the NRA depth profiles were completed, we also characterized the near-surface concentrations of Lu, P, and Li in the doped zircons. We mapped the surfaces of select

crystals using a laser ablation inductively coupled plasma mass spectrometer (LA-ICP-MS) which consisted of a Photon Machines 193-nm excimer laser attached to an Agilent 7900 quadrupole mass spectrometer hosted at the University of Rochester. A square laser spot size of 35 μm was used with a mass table consisting of ^{7}Li, Al, P, ^{139}La, ^{163}Dy, ^{175}Lu, ^{29}Si, and ^{91}Zr. The fluence was 7 mJ with the laser pulse rate set at 10 Hz and a raster speed of 17 μm/s. The He carrier gas for the Helix 2-volume cell had flow rates set at 0.6 (MFC1) and 0.2 (MFC2) liters per minute. The detection limits for the analytical protocol and instrument setup described here were ~1, ~7, and ~<1 ppm for Li, P, and the REEs, respectively. We temporally interspersed rasters of NIST 612 between zircon rasters. NIST612 rasters were used to calculate zircon concentrations by using ^{29}Si as an internal standard, and the element maps were produced with the Iolite 3.1 software package (Paul et al. 2012).

Implantation of Li into zircon

For the implantation experiments, slabs of Mud Tank zircon were oriented, cut with a diamond wafering blade, and then polished as described in the previous section. Samples were mounted on an aluminum plate and implanted with 80 keV ^{7}Li, produced in the Extrion ion implanter at the Ion Beam Laboratory at the University at Albany. Implant doses were 1×10^{15} Li/cm^2, leading to concentrations at peak for the implant dose of around 700 ppm by atom. Implanted samples were then placed in silica tubes with the oxygen fugacity buffered using the Ni + ½O_2 → NiO equilibrium reaction by placing a silica bucket filled with Ni + NiO powder directly inside the silica tube and sealing the assembly under vacuum. The oxygen fugacity buffer was physically separated from the zircon slab with pieces of silica glass but remained in chemical communication with the sample. Experiments conducted by this technique were either run at 800 or run at 650 °C. We confirmed the presence of both Ni and NiO at the end of each experiment. After completion of the diffusion experiment, samples were measured by NRA using the procedure outlined in the previous section. For the implanted samples, diffusivities were determined by using a model with an initial Gaussian distribution of the diffusant Li. For a semi-infinite medium, the concentration of diffusant is equal to zero at $x = 0$, and the distribution of the implanted species can be described as a function of depth (x) and time (t) after the solution of Ryssel and Ruge (1986):

$$C(x,t) = \frac{\frac{N_{imp}}{2\sqrt{\pi}}}{\sqrt{\left(1+\frac{2Dt}{\Delta R^2}\right)}} \left\{ \begin{array}{l} \exp\left[-\dfrac{(x-R)^2}{2\Delta R^2+4Dt}\right] \times \left[1+erf\left(\dfrac{\frac{R\sqrt{4Dt}}{\sqrt{2}\Delta R}+\frac{x\sqrt{2}\Delta R}{\sqrt{4Dt}}}{\sqrt{2\Delta R^2+4Dt}}\right)\right] \\ -\exp\left[-\dfrac{(x+R)^2}{2\Delta R^2+4Dt}\right] \times \left[1+erf\left(\dfrac{\frac{R\sqrt{4Dt}}{\sqrt{2}\Delta R}-\frac{x\sqrt{2}\Delta R}{\sqrt{4Dt}}}{\sqrt{2\Delta R^2+4Dt}}\right)\right] \end{array} \right\} \quad (2)$$

where D is the diffusion coefficient, N_{imp} is the maximum concentration of the implanted species in the unannealed sample (700 at. ppm), R is the range (depth in the material) of implanted species, and ΔR is the range straggle, which defines the width of the initial implanted distribution and is thus similar to the full width at half maximum of the Gaussian distribution. An unannealed piece of Li-implanted zircon was also analyzed by NRA, and its Li profile was fit to evaluate the parameters R and ΔR to use in fitting of Li profiles of annealed samples. The spectra of annealed samples were then fit to Eq. (2), holding R and ΔR constant; N_{imp} was allowed to vary by up to 20 %, commensurate with the propagated error on the concentration. Diffusivities were determined by implementing a nonlinear Levenberg–Marquardt iteration algorithm to obtain the best fits to the data.

Intra-grain Li diffusion

During the course of our reconnaissance studies, we discovered that, like the REEs, Li in zircon can exhibit sector zoning in synthetic zircons, where these early observations were based solely on LA-ICP-MS analysis and the symmetry of the crystal. Initial results revealed near-step-function Li concentration gradients from one sector to the next, at the ~20-μm resolution of the laser ablation spot. In order to evaluate whether Li migrates from one sector to the next, we first grew zircons as described above, except that ~300 ppm P and 1300 ppm Yb, and trace Dy were added at the same time—rather than independently—to produce zircons with a mixture of Li, P, and REEs. Dysprosium was a key addition because it is a known CL emitter in zircon, which therefore allows us to precisely image the sector boundary. After the experiment was completed, we extracted a 2 × 5 mm grain from the run product and then polished into the zircon to expose the sectors. These sectors were identified first by CL imaging, and then Li, P, and REE concentrations were characterized across sectors by LA-ICP-MS. This work was conducted at Rensselaer Polytechnic Institute using a Photon Machines 193-nm excimer laser connected to a Varian 820 MS quadrupole. Samples were analyzed with a laser fluence of 7 mJ, pulse rate of 10 Hz, and a laser spot size of 20 or 40 μm; a He carrier gas (flow rate = 0.7 liters per minute) was used to transport the analyte from the laser ablation sample chamber to the mass spectrometer. Laser ablation was carried out over a

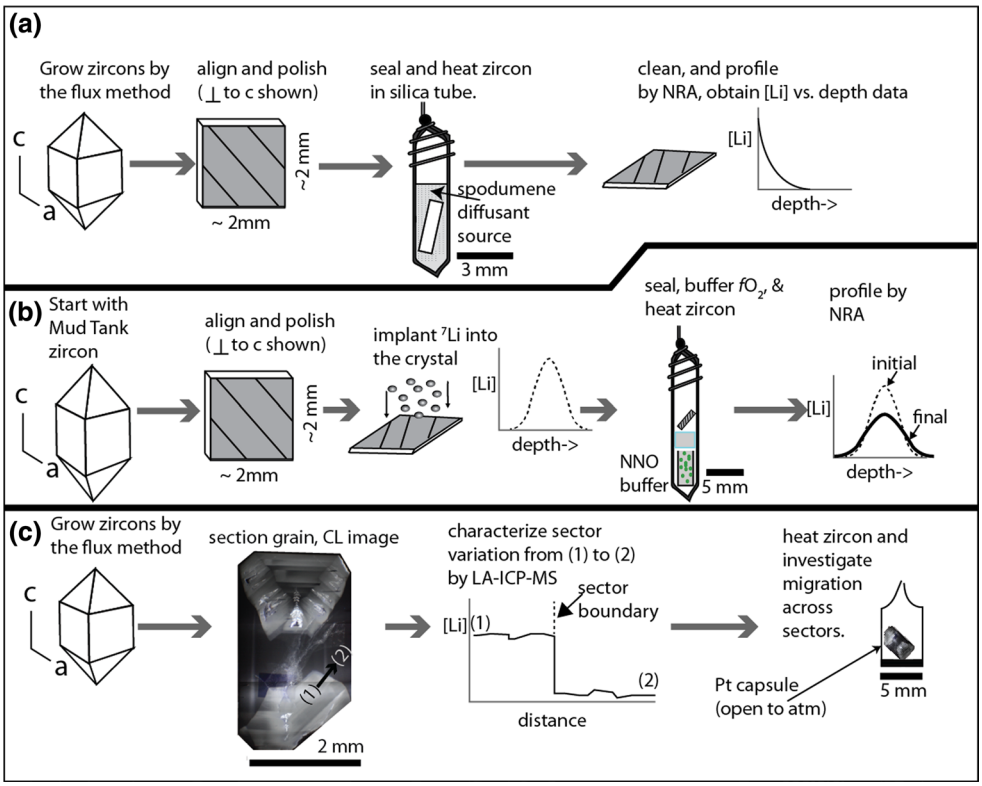

Fig. 1 Overview of the experimental setup for the three types of diffusion experiments conducted here. The CL image shown in (**c**) is from the actual grain investigated in this study

Table 1 Li diffusivities for zircon

Sample name	T (°C)	t (s)	D (m^2/s)	log (D)	±	Zircon source	Diffusion type	Crystal orientation	fO_2 buffer
ZLi21–undoped	920	86,400	7.20E−19	−18.14	0.06	Synthetic, "pure"	In diffusion	Polished//c	–
ZLi21-P-doped	920	86,400	7.18E−19	−18.14	0.05	Synthetic, P = ~400 ppm	In diffusion	Polished//c	–
ZLi21-Lu-doped	920	86,400	7.33E−19	−18.14	0.08	Synthetic, Lu = ~7000 ppm	In diffusion	Polished//a	–
ZLi22-Lu-doped	852	258,900	9.59E−20	−19.02	0.05	Synthetic, Lu = ~5000 ppm	In diffusion	Polished//a	–
ZLi22-P-doped	852	258,900	1.10E−19	−18.96	0.09	Synthetic, P ~200 ppm	In diffusion	Polished//c	–
ZLi23a	800	50,400	3.40E−19	−19.49	0.35	Mud Tank	Li implanted	Polished//c	Ni–NiO
ZLi23b	800	360,000	5.91E−20	−19.47	0.14	Mud Tank	Li implanted	Polished//c	Ni–NiO
ZLi24a	650	3,464,100	8.36E−22	−21.10	0.25	Mud Tank	Li implanted	Polished//c	Ni–NiO

~30-s counting period, with a background counting period of 35–45 s before and after each ablation (e.g., a total mass spectrometer counting period of 100–120 s). Mass ^{29}Si was used as an internal standard and unknown concentrations were determined using NIST612 glass (Pearce et al. 1997). Afterward, the same zircon was heated to 1500 °C for ~12 days in a 1 atmosphere furnace and the temperature was monitored with a type-S thermocouple (temperature uncertainty is ±5 °C). This should result in a Li diffusive length scale of ~100 μm (e.g., Cherniak and Watson 2010), assuming Li migrates independent of the REEs, which enables us to evaluate Li mobility with the 20-μm spatial resolution of a laser ablation spot. After heating, the grain surface was then re-analyzed by LA-ICP-MS. While the previously described linear accelerator-based characterizations are significantly more rigorous in regard to quantifying the diffusivities of Li in zircon, this approach enables us to test the end-member models in a different way; that is, does Li migrate independently of REEs, or are Li atoms inhibited from diffusing because of REEs? Figure 1 summarizes the basic experimental setup and concepts of each of the three techniques described here.

Results

Li in zircon depth profiling by NRA

Li diffusion coefficients are presented in Table 1, along with T, t, zircon orientation, and other experimental

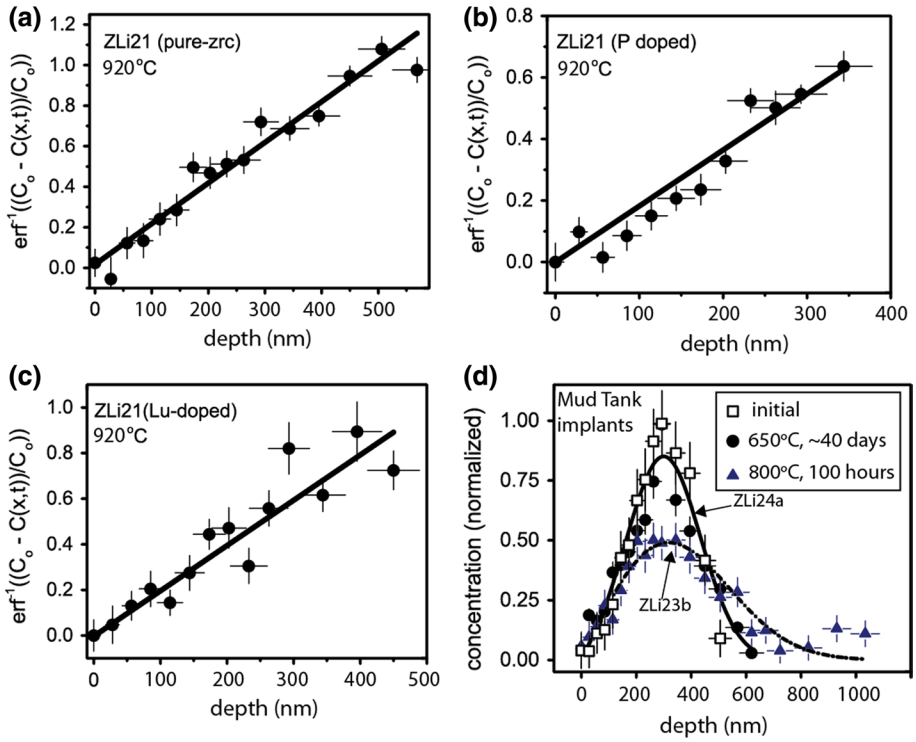

Fig. 2 **a–c** Results of diffusion profiles. A York regression was used to calculate the slope of the line, which is equal to $(4D{\cdot}t)^{-1/2}$. All three experiments were run under identical conditions; the only difference was the composition of the zircon (see Table 1 for reported diffusivities, and Fig. 5 for the impurity element concentrations). **d** Examples of initial Li implant (*square symbols*) and the relaxation of Gaussian profiles after heating; the diffusivities were calculated using Eq. 2 and the *curves* represent fits to the data

information. In Fig. 2a–c, we show examples of in-diffusion experiments for three different compositions that have been plotted as the inverse of the error function (i.e., $\mathrm{erf}^{-1}((C_o - C(x,t))/C_o)$) versus depth ($x$). In these three examples, zircon slabs were heated to 920 °C for 24 h. A York regression was used to calculate the slope of the line, which is equal to $(4D{\cdot}t)^{-1/2}$, and the resulting diffusivities for these three chemically diverse samples are identical within error, as reported in Table 1. Figure 2d shows an initial Li implantation in zircon, along with diffusion experiments conducted at 650 and 800 °C, where the relaxation of the Gaussian implants to determine the diffusivities were modeled using Eq. (2). In order to highlight the lack of dependence of diffusivities on compositional variations of the zircons, Fig. 3 plots diffusivities for the two in-diffusion temperature sets (~850 and 920 °C). We observe no resolvable differences in diffusivities within error for the "pure," Mud Tank, P-doped, or Lu-doped zircons.

Figure 4 summarizes all diffusivities on an Arrhenius plot, along with the diffusion data presented in Cherniak and Watson (2010). As noted, there are no observable differences in measured diffusivities as a function of zircon composition, and in addition, we obtain diffusivities for the implantation experiments that are consistent with the in-diffusion experiments. When only the data collected in this study are considered, which focused on the lower-temperature regime (920–650 °C), a York linear regression to the data yields an activation energy for diffusion of 273 ± 14 kJ/mol (slope) and a pre-exponential factor

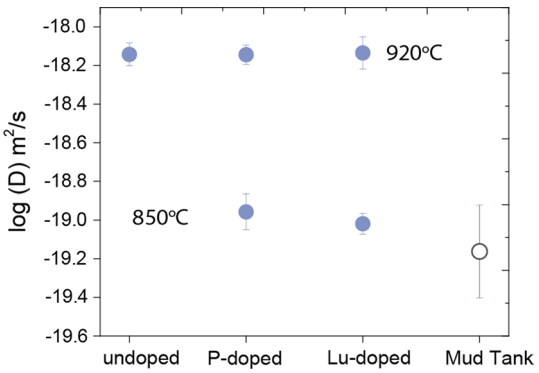

Fig. 3 Diffusivities plotted as a function of composition for two different temperatures. Data for the Mud Tank sample can be found in Cherniak and Watson (2010). *All data* represent the results of in-diffusion experiments

of 5.88×10^{-7} m²/s (y-intercept). Given the very strong agreement in measured diffusivities among all data—independent of zircon chemistry or implantation versus in-diffusion experiments—our preferred Arrhenius relationship incorporates the results of Cherniak and Watson (2010) and the data presented here, which results in an activation energy for diffusion of 278 ± 8 kJ/mol and a pre-exponential factor of 9.60×10^{-7}m²/s, yielding the following expression:

$$D_{\mathrm{Li}} = 9.60 \times 10^{-7} \exp\left[\frac{-278 \pm 8 \text{ kJ mol}^{-1}}{\mathrm{RT}}\right] \mathrm{m}^2\ \mathrm{s}^{-1} \quad (3)$$

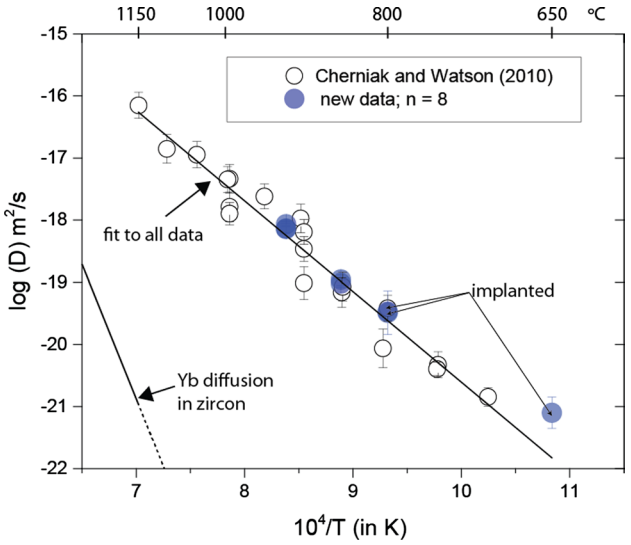

Fig. 4 Compilation of zircon Li diffusion data for this study and Cherniak and Watson (2010). The diffusivities calculated from the implanted experiments at 800 °C ($n = 2$) and 650 °C ($n = 1$) which are in agreement with the in-diffusion experiments. The Arrhenius line for Yb diffusion in zircon is from the results of Cherniak et al. (1997a)

Chemical composition of NRA-profiled zircons

In order to determine the REE + P contents of the synthetic zircons depth profiled for Li contents by the ~1 mm^2 NRA beamspot, we produced 2D maps of the near surface of the crystals used for in-diffusion experiments by LA-ICP-MS without polishing. These data were collected after the NRA Li depth profiles were completed (Fig. 5 and supplementary information). In the case of Lu-doped samples, Lu concentrations average ~6000–7500 ppm, but can be as high as ~10,000 ppm in some parts of the grain. The lowest Lu concentrations recorded are ~2500 and ~1000 ppm for samples ZLi21-Lu-doped and ZLi22-Lu-doped, respectively. Lutetium-doped samples have only trace amounts of P (~50 ppm), meaning that the potential for Li^+ charge balance with a trivalent cation during diffusion exists for these samples. Some maps revealed occasional Li-rich spots (e.g., see ZLi21-Lu-doped in Fig. 5). In this case, the Li-rich spot is approximately a factor of five higher than the average Li concentration measured by LA-ICP-MS (~170 ppm), but they make up less than 1 % of the surface area of the sample. Therefore, these regions of the grain have a negligible impact on the NRA surface depth profiles, which cover ~1 mm^2, and thus no corrections were deemed necessary. Phosphorus-doped samples have 300–500 ppm P in ZLi21-P-doped, while ZLi22-P-doped has a relatively uniform distribution of P at 200 ppm, except for the edge of the crystal, which contains 500–1500 ppm P. It should be noted that depth profilometry revealed that LA-ICP-MS rasters removed the outer ~5 μm of the surface of the sample, whereas NRA depth profiles only extended to a depth of ~500 nm. Nevertheless, we consider the concentration maps presented in Fig. 5 and supplementary information to be reasonable representations of the near surface of the crystal even though the LA-ICP-MS rasters sample an order of magnitude more volume. We did not map the surface of our undoped zircon (ZLi21-undoped), but instead it was analyzed by LA-ICP-MS in spot mode which yielded 7600, 12, and 55 ppm of Hf, Lu, and P, respectively. Thus, even though the zircons analyzed represent chemically diverse specimens, they yield statistically identical diffusivities.

Diffusion of Li across crystal sectors

Sector zoning is known to produce heterogeneous compositions in zircon. The preferred model used to describe this phenomenon here is caused by differences in the chemical potentials of specific elements in the near-surface regions of different crystallographic faces (Watson and Liang 1995). The magnitude of such effects—that is, the resulting differences in concentrations among sectors—appears to be highly dependent on the element and the mineral (e.g., Lanzillo et al. 2014; Trail et al. 2015). In the case of our synthetic flux-grown zircon (see the section on "Intra-grain Li diffusion" for experimental details), Li fractionation among sectors is very pronounced. For example, our initial characterization of the zircon reveals concentrations of ~30 ppm in one sector, which drops off steeply once the sector boundary is crossed to the limit of detection (~1 ppm). We exploited this difference, along with the sharp interface boundary, to conduct an intra-grain diffusion experiment.

Figure 6a presents results of three separate LA-ICP-MS spot traverses across the sector boundary; these data represent the initial characterization of this grain. The spot traverse locations are annotated on the inset figure of the zircon, which is represented by a backscattered scanning electron image of the area of interest, overlain by CL images (collected with a Gatan monoCL3 imaging system attached the Rensselaer Cameca SX-100 electron microprobe) so that the sector boundaries are clearly visible. The x-axes are defined relative to the sector boundary (that is, at the boundary, $x = 0$; negative numbers to the left, positive to the right). In addition to sector variations of Li contents, the right graph of Fig. 6a shows that Yb and P both exhibit sector zoning as well. Also note that the CL emitter Dy was included among the analyzed elements; values for this element decrease from 500 ppm to 300 ppm, from the bright to dark sector, respectively (see supplementary information). In the dark sector, an increase in P along with decrease in Yb + Dy contents implies that the charge-compensating reaction $REE^{3+} + Li^+ \rightarrow Zr^{4+}$ is less likely to occur, when compared to the bright sector. In fact, REE/P

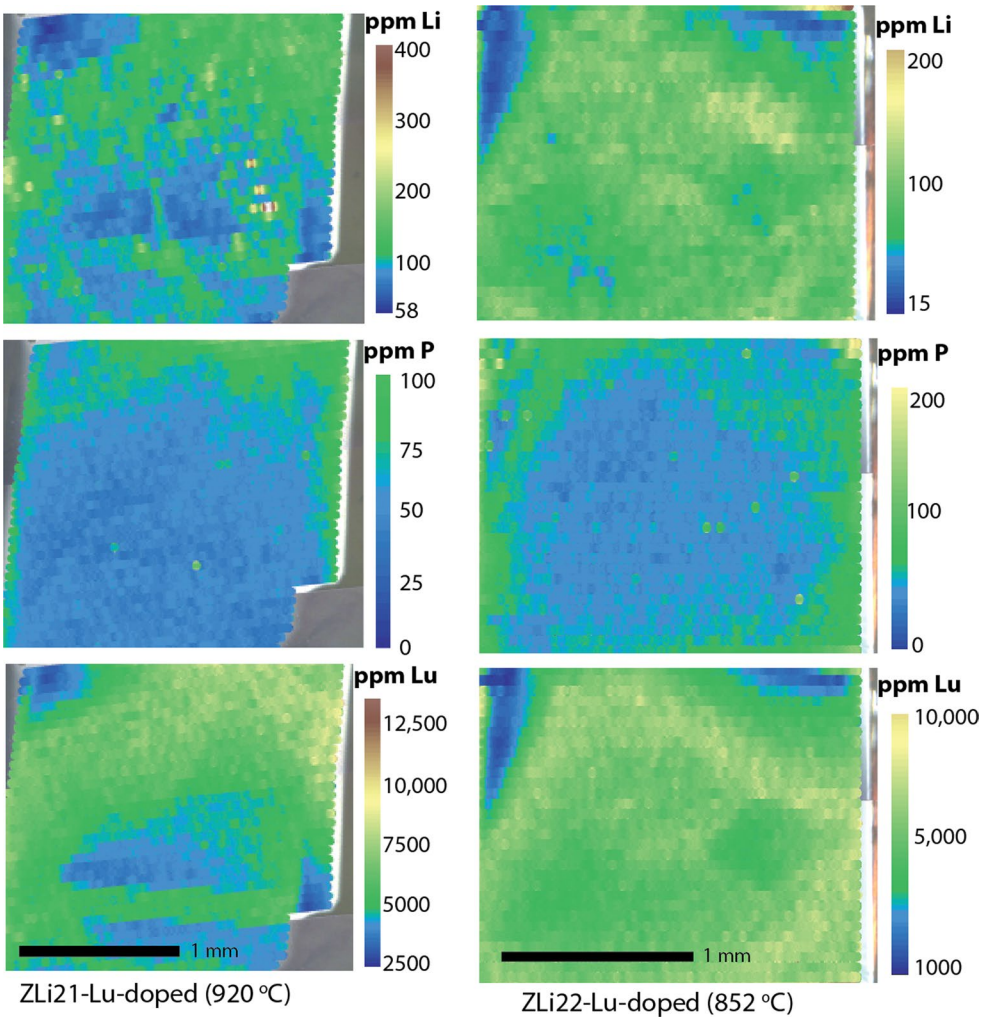

Fig. 5 Terrain maps showing the distribution of Li, P, and Lu within Lu-doped zircons. Most Lu concentrations on are in the range of 6000–7500 ppm, but ~1 wt% concentrations were also detected. ZLi22-Lu-doped shows evidence for sector zoning (also see the image for ZLi22-P-doped, which can be found in the supplementary data). Also note the broadly patterned correlation between Li and Lu in both samples, where high concentrations of Lu correspond to high concentrations of Li. In the case of ZLi22-Lu-doped, Li and P contents anti-correlate showing that both elements are—somewhat interchangeably—involved in charge compensation related to the entry of Lu^{3+} into the zircon structure and vice versa. Similar conclusions are reached for the laser ablation spot mode data presented for a different zircon in Fig. 6 as well

atomic ratios in the dark sector are greater than 1, whereas in the bright banded sector they are less than 1. This is consistent with the correlative decrease in Li in the dark sector relative to the bright sector.

After heating the grain to 1500 °C for 12 days and 3 h, we collected additional trace element data which are presented in Fig. 6b and 6c. Figure 6b represents additional analyses conducted on the exact same surface after the grain was heated. We placed the new LA-ICP-MS spot traverses close to or between the old spot traverses from the initial characterization. To illustrate this, the inset image in Fig. 6b shows black solid rectangles, which represents the locations of the initial grain characterization, whereas the annotated symbols on the crystal correspond to the data shown in Fig. 6b. Of immediate interest is the stark difference in measured Li contents after heating the zircon. Originally, the Li contents were high in the bright sector and below the detection limit in the dark sector, but after heating the crystal, the opposite is true. Specifically, Li contents are now at or below the 1 ppm detection limit in the bright sector, whereas Li contents in the dark sector range from below the detection limit near the sector interface up to ~6 ppm (at 100 μm from the sector interface). No detectable differences are observed when P, Dy, and Yb contents are compared from before and after heating.

Complementary to the results presented in Fig. 6b, which were collected on the surface of the crystal to a depth of the laser ablation pit, we present results in Fig. 6c which were obtained after ~100 μm was polished off the surface of the crystal. The bright sector still yields Li contents near the ~1 ppm detection limit, whereas the dark sector contains concentrations from ~2 to 5 ppm, consistent with the data presented in Fig. 6b. Ytterbium and P contents for this surface are broadly consistent with previously established concentration trends observed for the two sectors (i.e., Yb decreases from the bright sector to the dark, whereas the opposite trend is observed for P). While these data enable us to explore the mobility of Li initially coupled with REEs, this experiment is poorly constrained when compared to the data collected by NRA. We will discuss the meaning of these data in more detail in the discussion, but no attempt was made to calculate diffusivity for

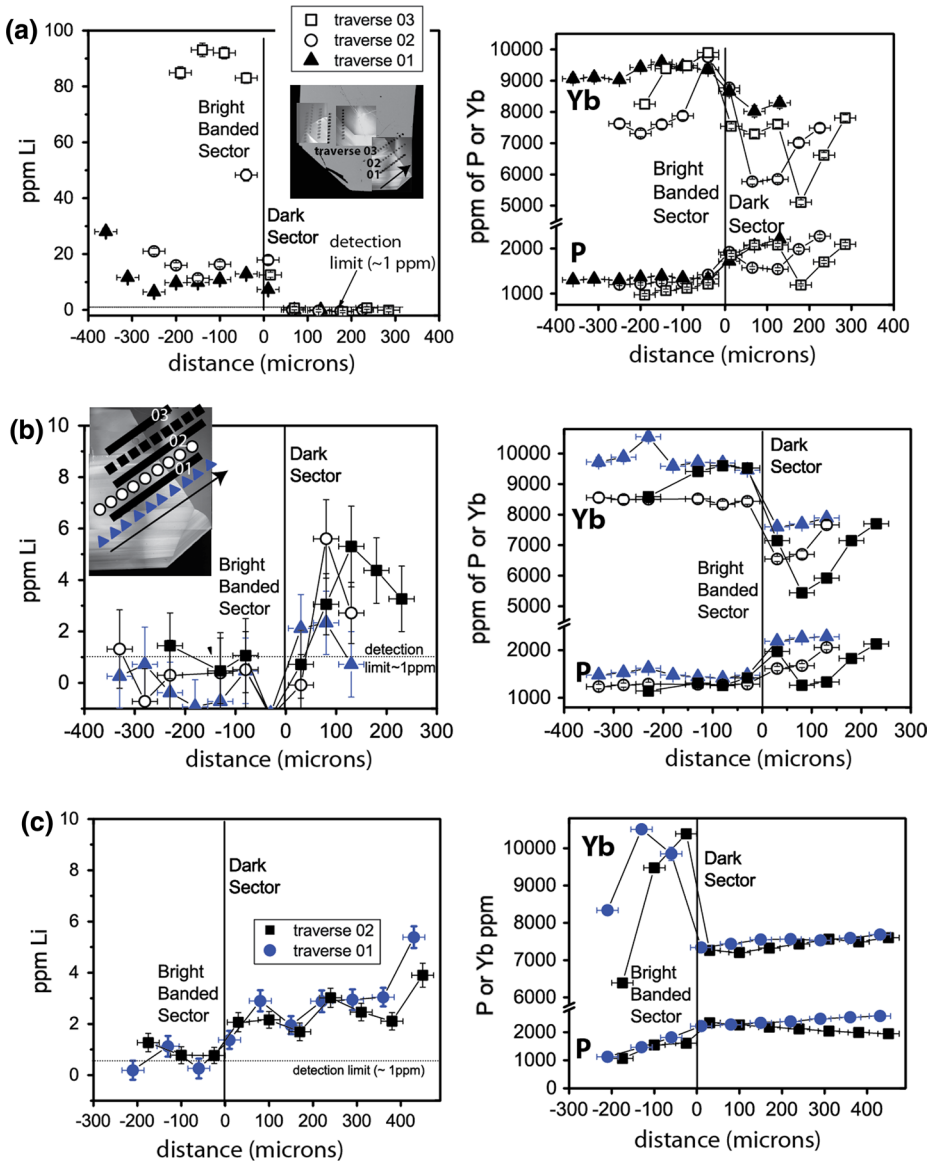

Fig. 6 Results of LA-ICP-MS data collected for spot traverses across the zircon sectors **a** Initial characterization of the synthetic zircon, showing differences in Li, Yb, and P across the zircon sectors. **b** Data collected on the same surface after heating the grain to 1500 °C for ~12 days. These traverses were placed close to or between the initial characterization traverses; see inset CL image. **c** Data were collected across the sector boundary, but after polishing into the crystal ~100 μm. In the case of (**a**) and (**b**) data were collected with a 20-μm spot, whereas the results in (**c**) were obtained with a 40-μm spot

this sample; rather the goal was to investigate in a different manner whether Li diffuses independent of REEs.

Discussion of experimental results

The diffusion data collected by NRA are, for the most part, straightforward to interpret: Despite the patterned features observed in the LA-ICP-MS maps, Li diffusivities obtained with NRA (where the beamspot interrogates a surface area of the sample ~1 mm^2) are in very strong agreement with previous Li in zircon diffusion results (Cherniak and Watson, 2010). Some of the zircons reported here (see supplementary information) yield surface concentrations an order of magnitude higher than 100 to 600 ppm at surface concentration values reported by Cherniak and Watson (2010), even though the diffusivities remain identical for both studies. Such observations suggest that the concentration of Li in zircon does not have an effect on its diffusion rate, even though the uptake of Li in zircon depends on the crystal chemistry. For example, the surface concentration of ZLi22-Lu-doped (852 °C) after the diffusion experiment was ~10^3 ppm at., which yielded log (D) [m^2/s] = -19.02 ± 0.05, whereas Cherniak and Watson (2010) reported a value of -19.16 ± 0.24 for trace-element-poor Mud Tank zircon heated to 851 °C. The above example also supports the model that Li diffusion in zircon does not depend on the REE composition of the zircon. We further illustrate this with a simple calculation: If Li was immobilized by REEs, then the Li diffusivity (at 920 °C) should be closer to 10^{-26} m^2/s (Cherniak et al. 1997a), but instead we measured a diffusivity (for zircon

ZLi21-Lu-doped) of ~10^{-18} m^2/s (Table 1). The different diffusivities predicted between these two end-member cases are easily detectable with the analytical techniques employed here. At the very least, high REE-bearing zircons do not result in sluggish diffusion of Li in synthetic zircons.

This conclusion was bolstered by the results of a single-grain heating experiment that might be more analogous to situations in which intra-grain variability and mobility of Li in minerals is the focus. Assuming a simple one-dimensional geometry and step function initial conditions, our 1500 °C heating step for ~12 days results in a diffusive length scale for Li of ~100 μm if Li is not immobilized by the REEs. The results of the experiment presented in Fig. 6 demonstrate that Li migrated on this order of magnitude, and importantly, there is no discernible change in the REEs or P, which leads to the conclusion that Li migrates independently of the REEs and P. Interestingly, we observed that Li migrates from across sectors during the heating event (e.g., Figure 6b); this is an intriguing feature that we discuss in some detail here.

In order to explain this, we need to distinguish between two separate, but important crystal characteristics. First, consider a zircon crystal growing in an environment where the chemical potential of Li in the near-surface region of two different crystal faces—e.g., (011) and (010)—is different. In this case, the (011) and (010) crystal growth surfaces yield different partition coefficients for Li; note that the "partition coefficients" we wish to define here represent the concentration at the very near surface of the crystal, divided by that in the melt. The strong sector zoning observed in our samples suggests that the zircon growth is sufficiently fast (and diffusion sufficiently slow) that the near-surface concentration was trapped within the lattice of the crystal. This resulted in initial Li, P, and Yb concentrations measured in different sectors that were demonstrably different. Second, when we heated the crystal, there must have existed a chemical potential for Li in order for the element to migrate from one sector to the other; in this case, the chemical potential was in the opposite direction of the initial concentration gradient.

In some respects, the role that REE + P plays in defining the chemical potentials for Li in zircon sectors—or in the case of oscillatory REE + P + Li growth zoning within a single sector—may be somewhat analogous to the partitioning and diffusion of trace elements in minerals that have major element concentration gradients. Plagioclase, for example, can show sharp step-function-like gradients in Li (Charlier et al. 2012) and Mg (Costa et al. 2003) between anorthite- and albite-rich regions in partially equilibrated samples. If the different chemical potentials of the trace elements between the two chemically distinct domains are not considered, then estimated $D{\cdot}t$ values from Li and Mg concentration gradients would be incorrect (Costa et al. 2003). However, these observations contain key differences to those made here for our zircon work. First, these studies identified Mg and Li compositional gradients correlating with anorthite mol% variations from 40 to 80, and 40 to 50 %, respectively (Costa et al. 2003; Charlier et al. 2012). In our zircon data, however, the minor element cation substitutions of REE for Zr and P for Si make up ~1 % or less of the cation sites in zircon. Second, Charlier et al. (2012) observed sharp step-function-like boundaries for Li on a spatial scale of ~10 or so microns, which correlated with the major element compositional changes of the plagioclase. However, our zircon Li concentration data after heating define a much smoother trend, where Li increases from near the detection limit up to maximum concentrations at ~100 μm from the compositional boundary interface. This smoother Li concentration trend—as shown in Fig. 6b—also contrasts with the sharper boundary that defined the initial state of the system (Fig. 6a).

Even so, if Li zoning in natural zircon samples is utilized as a geospeedometer and/or peak T indicator, we must evaluate whether Li concentrations correlate with the REEs and P in a manner that is consistent with zircon-melt/fluid partitioning related to zircon growth (e.g., the results in Fig. 6a satisfies this criterion, whereas the data in Fig. 6b violate it). If the sector-zoned case presented here can be used as a guide, then we predict that Li concentrations in zircon regions with atomic REE/P > 1 result from zircon-melt/fluid partitioning. In other words, Li zoning associated with atomic REE/P > 1 crystal regions—including "relaxed" Li profiles—represent promising target regions for geospeedometry or peak T studies. However, our observations indicate the Li zoning observed in zircon regions where atomic REE/P < 1—as is the case for the right dark sector in Fig. 6b—may be of limited value for geospeedometry studies. Until we understand equilibrium partitioning of Li as a function of REE ± P concentration, this idea cannot be addressed in additional detail.

These alternative explanations notwithstanding, we see no evidence in the present experimental work that demonstrates Li is immobilized by REEs. We also note that in natural settings, the charge-compensating reaction $H^+ + REE^{3+} \rightarrow Zr^{4+}$ has been documented (De Hoog et al. 2014); thus Li^+ and H^+ could commonly exchange for one another during heating events as dry conditions in the crust—that is, H-free environments—are presumably rare or absent altogether. In regard to natural zircons, Ushikubo et al. (2008) suggest their Li ion images of Jack Hills zircons reveal distinct zoning of Li, where Li zoning is observed on the scale of tens of microns. If we consider these data in the context of the main conclusion of our work—that is, that Li is not immobilized by charge compensation with REEs—then a plausible explanation for the observations made by Ushikubo et al. (2008) is that the zircons they investigated were not heated above 600 °C during

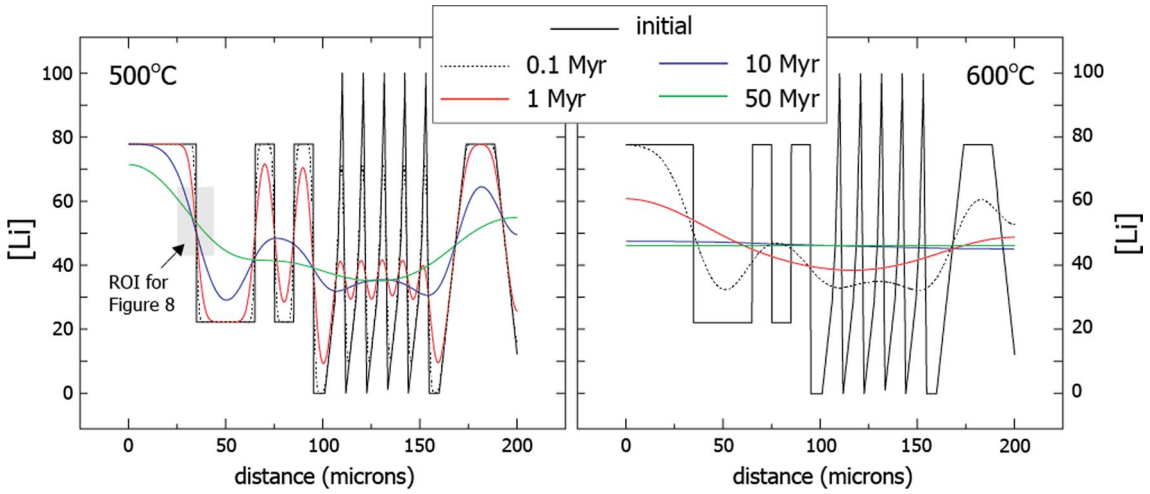

Fig. 7 Illustration of the effects of isothermal annealing at 500 and 600 °C on Li zoning in zircon. The *black lines* are the assumed initial zoning profile, which is deliberately complex to illustrate evolution of features at multiple length scales. Annealing times range from 0.1 to 50 Myr (see *line color* legend at the *top* of the figure). Note that at 600 °C even the shortest annealing time (100 kyr) leads to complete erasure of fine-scale features and major damping of larger-scale zoning; all zoning features are virtually eliminated in 1 Myr. At 500 °C, in contrast, the sharpest zoning features persist (with reduced amplitude) even at 1 Myr, and ~50-μm features are retained even at 10 Myr. The gray rectangle in the 500 °C panel denotes a region of interest where the slope of an actual diffusion profile could be used to quantify $D{\cdot}t$, as described in the text and illustrated in Fig. 8. Diffusive evolution of the Li profiles was computed in one dimension using a standard finite-difference method; the boundaries at 0 and 200 μm were considered to be zero-flux boundaries

their >4 Ga residence times in the crust. We will return to this idea in the next section.

One other feature of the sector-zoned data warrants discussion. It is clear that the total Li contents of the zircon appears to have decreased when the sector-zoned grain was heated—implying a net loss of Li from the zircon—as shown in Fig. 6. While we have insufficient data to speculate on the nature of the charge-compensating reaction involved here (e.g., loss of $2Li^+$ and O^{2-} would maintain charge balance), it is worth noting that loss of other monovalent cations in zircon during heating has been previously documented. Specifically, Trail et al. (2011b) presented FTIR data for synthetic zircon that showed that structurally bonded H was lost during heating of synthetic zircons, as determined by comparing absorption spectra in the OH bending region (e.g., 3000 to 3600 cm^{-1}) before and after heating the crystal. In this study, the integrated area decreased for both undoped and REE-doped zircon, suggesting that H^+ loss was not inhibited by charge compensation with a REE. For instance, in zircon doped with 1.33 wt % Lu_2O_3, the initial H_2O concentration was ~1300 ppm, whereas the concentrations after heating to 1000 °C for 64 h and 128 h were ~460 and ~200 ppm, respectively.

Applications to natural samples

In order to illustrate how the relaxation of a step-function-like Li concentration gradient in zircon might be used to reveal the thermal history of the grain, consider the ROI region in Fig. 7 for the 500 °C model. Further consider the case where Li diffusion has not affected the initial high and low concentration profiles (Eq. 3); for example, the 0.1 and 1 Myr heating durations at 500 °C would satisfy this criterion. In this particular case, a more general approach to using our Arrhenius parameters to relate Li diffusion to specific T-t conditions involves use of the midpoint slope, S_0, of a measured profile believed to be the result of diffusion in a natural crystal. For 1-D relaxation of a concentration step in an infinite medium, the midpoint slope (Fig. 8a; see Watson and Cherniak 2015) is a quantitative measure of $\int_0^t D(t)\mathrm{d}t$, or simply $D{\cdot}t$ for an isothermal diffusion episode. Specifically,

$$S_0 = \frac{C_h - C_l}{2\sqrt{\pi}\sqrt{D\Delta t}} \tag{4}$$

where C_h and C_l are the high and low plateau concentrations, respectively. Equation (4) is made completely general by normalizing the measured profile—by setting $C_h = 100$ and $C_l = 0$—as shown in Fig. 8a. In this case,

$$S_0 = \frac{28.21}{\sqrt{D\Delta t}} \tag{5}$$

Because $D = f(T)$, this relationship can be used to constrain the possible combinations of temperature and time capable of producing partial diffusive relaxation of an initial step profile in Li concentration like the one shown in Fig. 8a. Figure 8b is effectively a map of T–t conditions

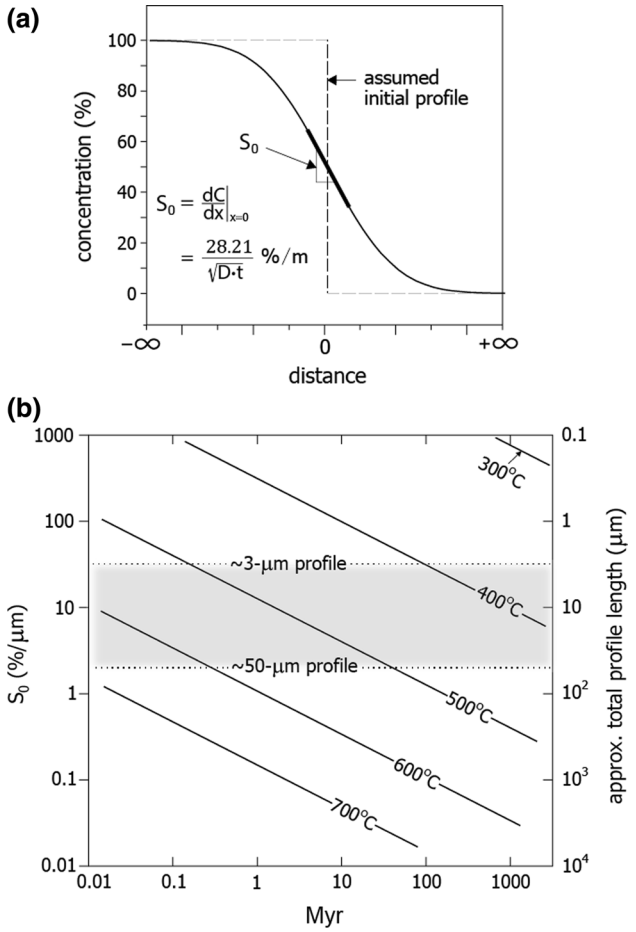

Fig. 8 **a** Partially relaxed step profile of Li concentration illustrating the significance of the midpoint slope S_0, which can be used to quantify the value of $D \cdot t$ required to produce an observed Li diffusion profile in zircon (see Eqs. 4, 5). To invoke S_0 for this purpose, the initial high and low concentration plateaus must be normalized to a difference of 100 % as shown on the figure (see text and Watson and Cherniak 2015); these plateaus must not have been "compromised" by diffusion for S_0 to be used quantitatively. (**b**) Graph illustrating S_0 as a function of time in Myr for isothermal annealing temperatures ranging from 300 to 700 °C. The *shaded gray region* shows the range of potential applicability of Li zoning profiles in zircon. Heating timescales less than 0.01 Myr are not particularly relevant for the main goal of our study, which focuses on subsolidus thermal events, but such short timescales but may be useful for investigating ~10- to ~100-year timescales of melt generation, storage, and eventual extraction of material during volcanic eruptions

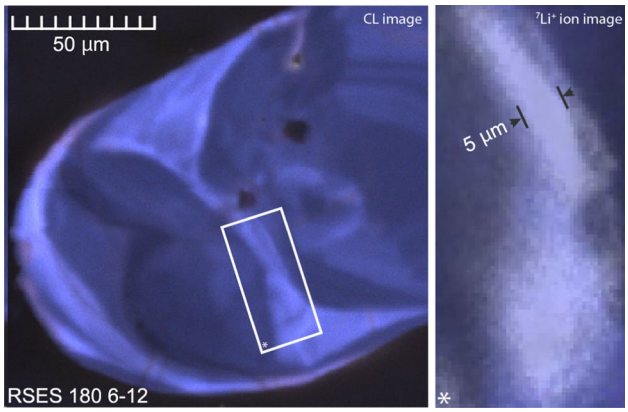

Fig. 9 Cathodoluminescence image of Jack Hills zircon RSES 180 6-12 showing complex internal zoning (*left*) with direct ion image of $^7Li^+$ (*right*). The strong correlation of Li with the narrow zone separating two regions of igneous character likely limits post-formation Li diffusion to length scales less than ~5 microns and thus to subsequent peak heating temperatures not exceeding 500 °C for ca. million-year timescales. This example reasonably constrains the discovery location of the Jack Hills Hadean zircons to having never reached amphibolite facies conditions or the Curie temperature of magnetite

required to produce a value of S_0 measured on a Li concentration profile. The shaded region in this figure represents the range of Li profiles that might be useful for zircon. This region is bounded at the top by the steepest slope (and shortest profile) that might be practical to measure (~3 μm; e.g., by SIMS ion imaging). The shaded region is bounded on the bottom by the shallowest slope (longest profile) likely to meet the infinite medium requirement in a natural zircon (~50 μm). Note that isotherms between 400 and 600 °C traverse the shaded region diagonally; at the high temperature end, however, a 600° event would have to be briefer than ~200 kyr to be successfully "recorded" (longer durations would create profiles unrealistically long for zircon). At the other extreme, 400° events leading to usable Li profiles would have durations ranging from ~100 Myr to greater than the age of the Earth.

One useful application of Fig. 8b will be to constrain the maximum temperature a specific zircon could have reached during a metamorphic event. If a zircon contained an initial step profile in Li concentration, this would tend to relax diffusively during a post-formation heating episode, acquiring slope S_0. If the value of S_0 were later measured in the laboratory to be 10 %/μm (for example), it is clear from Fig. 8b that a hypothetical heating event at 600 °C would generate this slope in only ~10 kyr. Because this duration is implausibly short for a geologic (tectonic) event, it would be reasonable to conclude that the zircon under consideration did not approach 600 °C after formation of the Li profile.

A final key point in reference to Eq. 4 and Fig. 8 is that use of S_0 to deduce information on *T–t* history yields *maximum T–t* parameters. This is so because it is assumed in this approach (for lack of a reasonable alternative) that the Li profile under consideration began as a sharp concentration step. If this were not in fact the case and the profile had a finite slope to begin with, then $D \cdot t$ of the actual thermal event would have to have been smaller than that indicated by S_0 through Eq. 4; that is, the temperature would have to have been lower and/or the time shorter.

In order to illustrate the potential usefulness of Li zoning in zircon as a peak T indicator, we present an example of a direct ion image of Li ($^{7}Li^{+}$) of the surface of a sectioned 4.03 Ga Jack Hills zircon, which contains a ~5-μm-high concentration band (Fig. 9). By broad analogy with Fig. 8, the general preservation of this band requires that peak heating temperature(s) for this detrital zircon did not exceed ~500 °C for million-year timescales. We emphasize that each detrital zircon from the Jack Hills or elsewhere must be evaluated individually; that is, each grain should be assumed to have a unique thermal history prior to deposition.

This ~5-μm-high concentration band enables a range of possible applications. For instance, it is unclear whether O isotopes in Hadean zircon record primary values, in part because of apparent disagreements in experimentally and naturally calibrated data for O diffusion in zircon. Watson and Cherniak (1997) characterized O diffusion in zircon and discovered that diffusion is demonstrably different for water-present (i.e., aqueous fluid pressures of 7–1000 MPa) versus dry conditions. Application of their water-present Arrhenius relationship reveals that core regions of zircons would be expected to retain primary oxygen isotope signatures only if post-crystallization temperatures did not exceed ~550–600 °C for million-year timescales. In contrast, Peck et al. (2003) empirically investigated oxygen isotope diffusion in zircon collected from amphibolite- and granulite-facies rocks of the Grenville Province and estimated closure temperatures in excess of 700 °C. While it seems clear that different groups will continue to use their preferred Arrhenius relationships to describe oxygen diffusion in zircon, sharp Li banding in zircon (e.g., Figure 9) and consideration of the caveats discussed in the previous section would allow researchers to confidently interpret the $^{18}O/^{16}O$ composition of Hadean zircons, independent of a preferred diffusivity.

With the exception of O, Li zoning in zircon will be of limited use to investigate the retention of other elements in zircon, though another important application involves the study of Hadean zircon inclusion mineralogy (see Hopkins et al., 2010 and Bell et al., 2015 for a review of primary inclusion mineralogy). In some cases, Hadean zircon inclusions appear to be isolated from visibly metamict or cracked gain regions, so diffusion of elements or isotope ratios in inclusions is likely to be rate limited by diffusion through the zircon lattice. Other inclusions that are associated with cracks could allow for isotopic or elemental exchange during metamorphism, if such cracks are not believed to be the result of sample preparation. In this example, a subsolidus peak T indicator for zircon may be of use to those who seek to investigate the chemistry of inclusions, especially if the element-of-interest closure temperature in an inclusion is comparable to thermally activated mobility of Li in zircon.

And finally, we undertook this investigation with a very specific application in mind. It is possible that the Jack Hills zircons and their ferromagnetic mineral inclusions may enable us to investigate the time of origin and earliest intensity of the Hadean magnetic field; it is now well established that there are ferromagnetic carriers in association with the Jack Hills sediments and the zircons themselves (e.g., Tarduno et al. 2015; Weiss et al. 2015). The timing and strength of the Hadean magnetic field has major implications for the thermal evolution of the Earth's interior, the physics of dynamo action, the evolution of the terrestrial atmosphere, and possibly the origin of life. If the oldest Jack Hills zircons are to provide any insight into the nature and state of Earth's early magnetic field, it will be necessary to establish that these crystals were not re-heated after their initial crystallization to temperatures above the Curie points of the inclusions carrying the magnetic record. For instance, if the magnetic carrier within zircon is magnetite, then it must be established that grains did not exceed 580 °C after igneous crystallization. However, a Hadean zircon's thermal history prior to the ~3.0-Ga deposition age is unknown. By analogy with Figs. 7 and 8, we propose that the distinct Li zoning observed in Fig. 9 provides a robust and best possible constraint for the peak (metamorphic) temperature for this zircon which we interpret to be approximately ~500 °C in our example. We note that this temperature estimate applies not only to the Jack Hills sediments, but also to the ~1-Ga crustal residence time of this grain prior to deposition in the Jack Hills. Thus, the zircon host rocks, and the zircons within them, have not been thermally re-magnetized above the magnetite Curie point, in agreement with peak metamorphic temperatures of ~346–487 °C inferred from Ti-in-quartz and monazite–xenotime thermometry (Rasmussen et al. 2010). Zircons that record Li features consistent with sub-Curie-point heating temperatures will be key targets for follow-up paleomagnetic measurements.

Summary and outlook

We investigated diffusivities of Li in chemically diverse samples by conducting diffusion studies in undoped, P-doped, and REE-doped zircon. We also implanted zircon with Li, leading to a Gaussian distribution at depth within the crystal, which we then relaxed by heating the grains in evacuated silica tubes with the oxygen fugacity buffered at the Ni–NiO equilibrium. We conducted a third type of experiment in which Li diffused across sector boundaries with different concentrations of REEs (and P). In all cases, we did not find evidence that Li mobility is impeded by REE charge compensation, and conclude that the Arrhenius relationship that should be used

to describe Li diffusion in zircon is independent of diffusivities determined for the REEs. These results are encouraging because it means that Li in zircon can be used as a geospeedometer to determine peak temperatures—or more specifically $D{\cdot}t$—that zircons experienced, assuming that Li is present and its initial zoning can be reasonably deduced to reflect the time of primary formation. Even though the main goal of our study emphasizes subsolidus heating events, Li zoning in zircon could also be utilized to investigate ~10- to ~100- year timescales of melt generation, storage, and eventual extraction of material during silicic volcanic eruptions.

Because Li exhibits sector zoning in synthetic zircon, such concentration boundaries within individual crystals may also become key targets in natural samples, keeping in mind some of the caveats presented in the discussion. While we do not unequivocally rule out some form of partial charge compensation with REEs as possibly inhibiting diffusion of Li in zircon in certain cases, our data suggest such immobility is an exception rather than the rule to be relied on when interpreting the meaning of Li concentration and isotope systematics in natural samples.

Acknowledgments This work was supported by the NASA Astrobiology Institute grant no. NNA09DA80A to RPI and by NSF Grant Nos. EAR-1447404 to D. Trail and EAR-0948204 to E.B. Watson. The ion microprobe facility at UCLA is partly supported by a grant from the Instrumentation and Facilities Program, Division of Earth Sciences, National Science Foundation. LA-ICP-MS work at RPI was made possible through the generosity of F. Dale Corman. We thank Ralf Dohmen, Takayuki Ushikubo, and an anonymous reviewer for their constructive comments. Ralf Dohmen in particular provided a very insightful review.

References

Bell EA, Boehnke P, Hopkins-Wielicki MD, Harrison TM (2015) Distinguishing primary and secondary inclusion assemblages in Jack Hills zircons. Lithos 234:15–26

Bouvier A-S, Ushikubo T, Kita NT, Cavosie AJ, Kozdon R, Valley JW (2012) Li isotopes and trace elements as a petrogenetic tracer in zircon: insights from Archean TTGs and sanukitoids. Contrib Mineral Petrol 163:745–768

Chan LH, Edmond JM, Thompson G, Gillis K (1992) Lithium isotopic composition of submarine basalts: implications for the lithium cycle in the oceans. Earth Planet Sci Lett 108:151–160

Charlier BLA, Morgan DJ, Wilson CJN, Wooden JL, Allan ASR, Baker JA (2012) Lithium concentration gradients in feldspar and quartz record the final minutes of magma ascent in an explosive supereruption. Earth Planet Sci Lett 319–320:218–227

Chase AB, Osmer JA (1966) Growth and preferential doping of zircon and thorite. J Electrochem Soc 113:198–199

Cherniak DJ, Watson EB (2001) Pb diffusion in zircon. Chem Geol 172:5–24

Cherniak DJ, Watson EB (2007) Ti diffusion in zircon. Chem Geol 242:473–486

Cherniak DJ, Watson EB (2010) Li diffusion in zircon. Contrib Mineral Petrol 160:383–390

Cherniak DJ, Hanchar JM, Watson EB (1997a) Rare-Earth diffusion in zircon. Chem Geol 134:289–301

Cherniak DJ, Hanchar JM, Watson EB (1997b) Diffusion of tetravalent cations in zircon. Contrib Mineral Petrol 127:383–390

Costa F, Chakraborty S, Dohmen R (2003) Diffusion coupling between trace and major elements and a model for calculation of magma residence times using plagioclase. Geochim Cosmochim Acta 67:2189–2200

Crank J (1975) The mathematics of diffusion. Clarendon Press, Oxford

D'Agostino MD, Kamykowski EA, Kuehne FJ, Padawer GM, Schneid EJ, Schulte RL, Stauber MC, Swanson FR (1978) Nuclear techniques for bulk and surface analysis of materials. J Radioanal Chem 43:421–438

De Hoog JCM, Lissenberg CJ, Brooker RA, Hinton R, Trail D, Hellebrand EWG, Brooker RA (2014) Hydrogen incorporation and charge balance in natural zircon. Geochim Cosmochim Acta 141:472–486

Dohmen R, Kasemann SA, Coogan L, Chakraborty S (2010) Diffusion of Li in olivine. Part I: experimental observations and a multi species diffusion model. Geochim Cosmochim Acta 74:274–292

Elliott T, Thomas A, Jeffcoate A, Niu Y (2006) Lithium isotope evidence for subduction-enriched mantle in the source of midocean-ridge basalts. Nature 443:565–568

Grimes CB, Ushikubo T, John B, Valley JW (2011) Uniformly mantle like $\delta^{18}O$ in zircons from oceanic plagiogranites and gabbros. Contrib Mineral Petrol 161:13–33

Grimes CB, Wooden JL, Cheadle MJ, John BE (2015) "Fingerprinting" tectono magmatic provenance using trace elements in igneous zircon. Contrib Mineral Petrol 170:46

Hanchar JM, Finch RJ, Hoskin PWO, Watson EB, Cherniak DJ, Mariano AM (2001) Rare earth elements in synthetic zircon: Part 1. Synthesis, and rare earth element and phosphorus doping. Am Mineral 86:667–680

Harrison TM, Schmitt AK, McCulloch MT, Lovera OM (2008) Early (≥4.5 Ga) formation of terrestrial crust: Lu–Hf, δ18O, and Ti thermometry results for Hadean zircons. Earth Planet Sci Lett 268:476–486

Hopkins MD, Harrison TM, Manning CE (2010) Constraints on Hadean geodynamics from mineral inclusions in >4 Ga zircons. Earth Planet Sci Lett 298:367–376

Jeffcoate AB, Elliott T, Kasemann SA, Ionov D, Cooper K, Brooker R (2007) Li isotope fractionation in peridotites and mafic melts. Geochim Cosmochim Acta 71:202–218

Lanzillo NA, Watson EB, Thomas JB, Nayak SK, Curioni A (2014) Near-surface controls on the composition of growing crystals: Car-Parrinello molecular dynamics (CPMD) simulations of Ti energetics and diffusion in alpha quartz. Geochim Cosmochim Acta 131:33–46

Li X-H, Li Q-L, Liu Y, Tang G-Q (2011) Further characterization of M257 zircon standard: a working reference for SIMS analysis of Li isotopes. J Anal At Spectrom 26:352–358

Magna T, Wiechert U, Halliday AN (2006) New constraints on the lithium isotope compositions of the Moon and terrestrial planets. Earth Planet Sci Lett 243:336–353

Mojzsis SJ, Harrison TM, Pidgeon RT (2001) Oxygen-isotope evidence from ancient zircons for liquid water at the Earth's surface 4300 Myr ago. Nature 409:178–181

Paul B, Paton C, Norris A, Woodhead J, Hellstrom J, Hergt J, Greig A (2012) Cell Space: A module for creating spatially registered laser ablation images within the Iolite freeware environment. J Anal At Spectrom 27:700–706

Pearce NJG, Perkins WT, Westgate JA, Gorton MP, Jackson SE, Neal CR, Chenery SP (1997) A compilation of new and published major and trace element data for NIST SRM 610 and NIST SRM 612 glass reference materials. Geostand Newsl J Geostand Geoanalysis 21:115–144

Peck WH, Valley JW, Graham CM (2003) Slow oxygen diffusion rates in igneous zircons from metamorphic rocks. Am Mineral 88:1003–1014

Raisanen J, Lappalainen R (1986) Analysis of lithium using external proton beams. Nucl Instrum Methods B15:546–549

Rasmussen B, Fletcher IR, Muhling JR, Wilde SA (2010) In situ U-Th–Pb geochronology of monazite and xenotime from the Jack Hills belt: implications for the age of deposition and metamorphism of Hadean zircons. Precambrian Res 180:26–46

Richter FM, Watson EB, Chaussidon M, Mendybaev R, Ruscitto D (2014) Lithium isotope fractionation by diffusion in minerals. Part 1: Pyroxenes. Geochim Cosmochim Acta 126:352–370

Rubin A, Cooper KM, Kent AJ, Costa Rodriguez F, Till CB (2014) Using Li diffusion to track thermal histories within single zircon crystals. Abstract V31F-02 presented at 2014 Fall Meeting, AGU, San Francisco, Calif., 15–19 Dec

Ryssel H, Ruge I (1986) Ion implantation. Wiley, London

Seitz H-M, Brey GP, Lahaye Y, Durali S, Weyer S (2004) Lithium isotopic signatures of peridotite xenoliths and isotopic fractionation at high temperature between olivine and pyroxenes. Chem Geol 212:163–177

Suzuki K, Kouta H, Nagasawa H (1992) Hf–Zr interdiffusion in single crystal zircon. Geochem J 26:99–104

Tarduno JA, Cottrell RD, Davis WJ, Nimmo F, Bono RK (2015) A Hadean to Paleoarchean geodynamo recorded by single zircon crystals. Science 349:521–524

Tomascak PB, Langmuir CH, le Roux PJ, Shirey SB (2008) Lithium isotopes in global mid-ocean ridge basalts. Geochim Cosmochim Acta 72:1626–1637

Trail D, Watson EB, Tailby ND (2011a) The oxidation state of Hadean magmas and implications for early Earth's atmosphere. Nature 480:79–82

Trail D, Thomas JB, Watson EB (2011b) The incorporation of hydroxyl into zircon. Am Mineral 96:60–67

Trail D, Tailby ND, Lanzirotti A, Newville M, Thomas JT, Watson EB (2015) Magma redox evolution of silicic magmas: insights from high spatial resolution Ce^{4+}/Ce^{3+} measurements of single Bishop Tuff zircons. Chem Geol 402:77–88

Ushikubo T, Kita NT, Cavosie AJ, Wilde SA, Rudnick RL, Valley JW (2008) Lithium in Jack Hills zircons: Evidence for extensive weathering of Earth's earliest crust. Earth Planet Sci Lett 272:666–676

Watson EB, Cherniak DJ (1997) Oxygen diffusion in zircon. Earth Planet Sci Lett 148:527–544

Watson EB, Cherniak DJ (2015) Quantitative cooling histories from stranded diffusion profiles. Contrib Mineral Petrol 169:1–14

Watson EB, Harrison TM (2005) Zircon thermometer reveals minimum melting conditions on earliest Earth. Science 308:841–844

Watson EB, Liang Y (1995) A simple model for sector zoning in slowly-grown crystals: Implications for growth rate and lattice diffusion, with emphasis on accessory minerals in crustal rocks. Am Mineral 80:1170–1187

Weiss BP, Maloof AC, Tailby N, Ramezani J, Fu RR, Hanus V, Trail D, Watson EB, Harrison TM, Bowring SA, Kirschvink JL, Swanson-Hysell NL, Coe RS (2015) Pervasive remagnetization of detrital zircon host rocks in the Jack Hills, Western Australia and implications for records of the early geodynamo. Earth Planet Sci Lett 430:115–128

Wilde SA, Valley JW, Peck WH, Graham CM (2001) Evidence from detrital zircons for the existence of continental crust and oceans on the Earth 4.4 Gyr ago. Nature 409:175–178

Ziegler JF, Biersack JP (2006) The stopping and range of ions in matter. Computer code SRIM 2006. http://www.srim.org